Stellar electron-capture rates on nuclei based on a microscopic Skyrme functional

Fantina, A. F.; Khan, E.; Colo, G.; Paar, Nils; Vretenar, Dario

Journal article, Published version
Rad u časopisu, Objavljena verzija rada (izdavačev PDF)

Permanent link / Trajna poveznica: https://urn.nsk.hr/urn:nbn:hr:217:681047

Download date / Datum preuzimanja: **2024-05-03**

Repository / Repozitorij:

Repository of the Faculty of Science - University of Zagreb

Stellar electron-capture rates on nuclei based on a microscopic Skyrme functional

A. F. Fantina,[1] E. Khan,[2] G. Colò,[3] N. Paar,[4] and D. Vretenar[4]

[1]*Institut d'Astronomie et d'Astrophysique, CP226, Université Libre de Bruxelles, B-1050 Brussels, Belgium*
[2]*Institut de Physique Nucléaire, Université Paris-Sud, IN2P3-CNRS, 91406 Orsay Cedex, France*
[3]*Dipartimento di Fisica dell'Università degli Studi and INFN, Sezione di Milano, via Celoria 16, 20133 Milano, Italy*
[4]*Physics Department, Faculty of Science, University of Zagreb, Croatia*

We compute electron-capture rates for ^{54,56}Fe and Ge isotopes using a self-consistent microscopic approach. The single-nucleon basis and the occupation factors in the target nucleus are calculated in the finite-temperature Skyrme Hartree-Fock model, and the $J^\pi = 0^\pm$, $1^\pm$, $2^\pm$ charge-exchange transitions are determined in the finite-temperature random-phase approximation (RPA). The scheme is self-consistent; i.e., both the Hartree-Fock and the RPA equations are based on the same Skyrme functional. Several interactions are used in order to provide a theoretical uncertainty on the electron-capture rates for different astrophysical conditions. Comparing electron-capture rates obtained either with different Skyrme sets or with different available models indicates that differences up to one to two orders of magnitude can arise.

I. INTRODUCTION

Weak interaction processes play a pivotal role in the life of a star, especially during the late stages of the evolution of massive stars [1,2]. During the pre-supernova stage, the competition between β decay,

$$(Z, N) \longrightarrow (Z + 1, N - 1) + e^- + \bar{\nu}_e, \tag{1}$$

and electron capture,

$$(Z, N) + e^- \longrightarrow (Z - 1, N + 1) + \nu_e, \tag{2}$$

determines the core entropy and the electron fraction Y_e, which defines the mass of the inner core. Such a core, at the end of the hydrostatic chain of nuclear burning, is stabilized by the electron degeneracy pressure, until its mass does not exceed the Chandrasekhar mass $M_{Ch} \propto Y_e^2$ ($M_{Ch} \approx 1.4 M_\odot$). If this mass limit is exceeded, the electron pressure is no longer able to sustain the core, which collapses under the gravitational force, starting the so-called core-collapse supernova. During the supernova core collapse, electron capture on free protons and on exotic nuclei controls the neutronization phase, until the formation of an almost deleptonized central compact object, the neutron star. For matter densities $\rho \lesssim 10^{11}$ g cm^{-3}, neutrinos escape from the star, carrying away energy and contributing toward a decrease in the lepton number, thus accelerating the collapse. The rising density increases the neutrino diffusion time scale and, for densities $\gtrsim 10^{12}$ g cm^{-3}, neutrinos become trapped, driving the system toward β equilibrium.

Electron capture and β decays are dominated by Gamow-Teller (GT) and Fermi transitions. While the cross section for the electron capture on free protons is well known, computing that on nuclei is not a straightforward task in nuclear structure. For initial $Y_e \approx 0.5$, electron capture dominates over β decay, since the degenerate gas of electrons blocks the phase space available for decay, but the two processes become competitive as the matter becomes more neutron rich [2,3]. Moreover, because of finite-temperature effects, excited states can be thermally populated and their connection to the low-lying

states in the daughter nucleus by the GT transitions can contribute to the β-decay rates. In the early stage of the collapse, for densities below a few 10^{10} g cm^{-3} and temperatures between 300 and 800 keV, electron capture mainly occurs on nuclei with mass number $A \leqslant 60$. Therefore, the electron chemical potential μ_e is of the same order of magnitude as the nuclear Q value, and electron-capture cross sections are sensitive to the details of the GT strength distribution. With increasing density and temperature during collapse, the electron capture occurs on nuclei with $A > 65$, and the electron chemical potential is higher than the nuclear Q value. Thus, the capture rates are mainly determined by the centroid and the total GT strength. Around neutrino trapping, the electron chemical potential reaches values of around 30 MeV, and the forbidden transitions can no longer be neglected [2,3].

Because of the great importance of the weak interaction rates in astrophysical applications, they were extensively investigated within various approaches. For about fifteen years, the reference rates for electron and positron capture, β decay, and positron emission for nuclei in $21 \leqslant A \leqslant 60$ were those computed by Fuller, Fowler, and Newman [4]. They were based on the independent-particle model (IPM) using experimental information whenever available. New experimental data carried out in the iron mass region (see, e.g., Ref. [5]) showed that the GT transitions are quenched with respect to the calculations based on the IPM and fragmented over many states in the daughter nucleus, because of the effect of the residual interaction which is neglected in the IPM. Then, Caurier *et al.* [6] performed shell-model (SM) calculations for iron group nuclei. Their results agreed quite well with the data, showing that the SM was a good tool to calculate electron-capture rates. Evaluation of electron-capture rates has been improved for Ni isotopes with the use of the new SM Hamiltonian, GXPF1J [7]. The calculations performed in Ref. [7] reproduce quite well the observed GT$^+$ strengths and the capture rates obtained by experimental $B(GT^+)$ values, especially in ^{60}Ni, as well as the experimental energy position of the GT strength in ^{62}Ni

and the experimental GT strength of the transition $^{64}Ni \rightarrow$ ^{64}Co. The large-scale shell model Monte Carlo (SMMC) method was applied to compute β^+ and β^- decay rates for stellar conditions for more than 100 nuclei in the mass range $A = 45$–65 [8–10]. Using the improved rates, pre-supernova models were recomputed by Heger *et al.* [11], who found changes in the core Y_e and entropy, which, in turn, can have important consequences for the supernova and nucleosynthesis evolution. However, the SM diagonalization cannot be applied for nuclei beyond the *pf* shell, if configuration mixing and finite-temperature effects are included, because of the huge dimension of the model space involved. To overcome this problem, Langanke *et al.* [12] proposed the so-called hybrid model. In this approach, the calculation of the capture rates is performed in two steps: (i) the nucleus is described by a Slater determinant with temperature-dependent occupation numbers, determined within the SMMC framework; (ii) the capture rates are calculated from the GT strength distribution computed with the random-phase approximation (RPA) built on top of the Slater determinant. Using the SMMC + RPA hybrid model, electron-capture rates for about 200 nuclei in the mass range $A = 65$–112 were computed, for typical densities and temperatures encountered in supernova collapse [13]. Even if the electron-capture rates on free protons are larger than those on nuclei, the free protons abundance is low during collapse. Therefore, it has been found that the electron capture on nuclei dominates over the capture on free protons during the collapse phase, leading to significant changes in the supernova dynamics and collapse trajectories (see, e.g., Refs. [2,3]).

The SMMC + RPA hybrid model has been more recently applied to compute electron-capture rates for 170 additional nuclei, up to $A = 120$ [14]. Furthermore, in Ref. [14], the calculation of the electron-capture rates for stellar conditions has been extended to an additional 2200 nuclei in the range $Z = 28$–70 and $N = 40$–160. Because of the prohibitive computation time required by the SMMC calculations, Juodagalvis *et al.* [14] proposed a Fermi-Dirac parametrization to compute the fractional occupation number of the various shells in the ground state of the parent nucleus.

Recently, mean-field-based models have been used for the prediction of electron-capture cross sections and rates. A finite-temperature charge-exchange RPA model based on Skyrme functionals has been applied in Ref. [15] to predict electron-capture cross sections using several interactions. A similar approach, extended to the relativistic framework, has been employed in Ref. [16]. In the latter work, electron-capture rates for astrophysical conditions have also been computed, and similar trends for both cross sections and rates have been observed with respect to previous calculations. However, in Ref. [16], only one functional, the DD-ME2 parametrization, has been used. A thermal quasi-particle RPA approach (TQRPA), based on the Woods-Saxon potential and separable multipole and spin-multipole particle-hole interactions, has been applied in Ref. [17]. The finite-temperature effects are taken into account using the thermofield dynamics formalism. Although not as consistent as the one in Refs. [15] and [16], this approach allows one to account for effects beyond the RPA level. In this family of models, the prediction of electron-capture rates using Skyrme interactions remains to be done.

In the present work we use the self-consistent model introduced in Ref. [15], based on finite-temperature charge-exchange RPA, to predict electron-capture rates. The single-nucleon basis and the occupation factors in the target nucleus are calculated in the finite-temperature Skyrme Hartree-Fock (FTSHF) model, and the charge-exchange transitions are determined in the finite-temperature RPA (FTRPA) framework. The specificity and the advantage of this approach is that a FTSHF + FTRPA model is completely determined by the choice of the nuclear interaction employed; i.e., both the single-nucleon Hartree-Fock equations and the RPA matrix equations are based on the same Skyrme functional. Therefore, the calculation can be extended over arbitrary mass regions of the nuclide chart without additional assumptions or adjustment of the parameters. This represents a step forward toward a universal description of the electron-capture rates. The use of several Skyrme functionals with various properties also allows one to estimate the theoretical uncertainty on the electron-capture cross section and rates, which is of relevant importance for astrophysical application. In this work, we also aim at estimating this uncertainty.

The paper is organized as follows: in Sec. II the framework and the formalism of the FTSHF + charge-exchange FTRPA to calculate cross sections for electron capture will be recalled. In Sec. III and IV the cross sections and the rates for electron capture on $^{54,56}Fe$ and on neutron-rich germanium isotopes will be investigated. Finally, in Sec. V, we will give our conclusions and outlook.

II. FORMALISM

The formalism for the electron-capture cross section calculation with the Skyrme FTRPA approach has been detailed in Ref. [15]. Therefore, here, we only recall the main points, and we shall focus on the calculation of the electron-capture rates.

For the purposes of the present study, the Hartree-Fock (HF) model based on Skyrme functionals at finite temperature [18] is used to determine the single-nucleon spectra, occupation probabilities, and wave functions of the initial state of target nuclei. The occupation numbers are introduced by Fermi distributions, and the chemical potential is calculated using the particle conservation equation. For the description of the transitions relevant in electron capture on nuclei, the charge-exchange FTRPA is used. The effective interactions in the FTSHF + FTRPA are included in a consistent way; i.e., both in the ground-state calculations and in the equations of FTRPA the same Skyrme functional has been employed. The FTRPA equations are derived in the matrix form adopted from Ref. [19].

The nuclei that will be considered in this work contribute to stellar electron-capture rates in the temperature interval $0.5 < T < 2$ MeV. The expression for the total cross section for electron capture on a nucleus (Z, N) at temperature T reads

$$\sigma(E_e, T) = \frac{G_F^2}{2\pi} \sum_i F(Z, E_e) \frac{(2J_i + 1)e^{-E_i/(kT)}}{G(Z, A, T)}$$
$$\times \sum_{f,J} (E_e - Q + E_i - E_f)^2 \frac{|\langle i|\hat{O}_J|f\rangle|^2}{(2J_i + 1)}, \quad (3)$$

where $G_F = G_F/(\hbar c)^2$ is the Fermi coupling constant, E_e is the energy of the incoming electron, Q is the Q value of the reaction, J is the total angular momentum, and $\hat{O}_J$ is the generic notation for the charge $\hat{\mathcal{M}}_J$, longitudinal $\hat{\mathcal{L}}_J$, transverse electric $\hat{\mathcal{T}}_J^{\text{EL}}$, and transverse magnetic $\hat{\mathcal{T}}_J^{\text{MAG}}$ multipole operators. Detailed expressions for these operators are given in Refs. [20–22]. The sum over initial states includes a thermal average of levels, with the corresponding partition function $G(Z, A, T)$. The Fermi function $F(Z, E_e)$ corrects the cross section for the distortion of the electron wave function by the Coulomb field of the nucleus [23]. The finite temperature induces the thermal population of excited states in the parent nucleus (labeled as "i"), which are connected by the multipole operators to many levels in the daughter nucleus (labeled as "f"). The calculation of all possible transitions is computationally prohibitive; therefore, the evaluation of the total cross section for electron capture is usually simplified [4,8,12] by adopting the Brink hypothesis, that is, by assuming that the strength distribution of the multipole operators in the daughter nucleus is the same for all initial states and shifted by the excitation energy of the initial state. By using this approximation, the sum over final states becomes independent of the initial state and the sum over the Boltzmann weights cancels the partition function. The Brink hypothesis is a valid approximation when the temperature and the density are high enough so that many states contribute and variations in the low-energy transition strength cancel out. As was previously done in the calculation of stellar electron capture [12,15], we apply the Brink hypothesis to the initial state, which represents the thermal average of many-body states in the parent nucleus at temperature T. With this approximation, the final expression for the total electron-capture cross section at T reads [15]

$$\sigma(E_e, T) = \frac{G_F^2}{2\pi} F(Z, E_e) \sum_f (E_e - Q - \omega_f)^2 \sum_J S_J(\omega_f, T),$$

(4)

where ω_f is the excitation energy in the daughter nucleus, and S_J is the discrete finite-temperature RPA response for the multipole operator $\hat{O}_J$. In order to evaluate the electron-capture cross sections of Eq. (4), for each transition operator $\hat{O}_J$ the matrix elements between the initial state of the even-even (N, Z) target nucleus and the final state in the corresponding $(N + 1, Z - 1)$ nucleus are expressed in terms of single-particle matrix elements between the single-particle states and the corresponding FTRPA amplitudes (see Eq. (30) and Sec. II A in Ref. [15]):

$$\langle J_f \| \hat{O}_J \| J_i \rangle = \sum_{\alpha\beta} \langle \alpha \| \hat{O}_J \| \beta \rangle \left(\delta\rho_{\alpha\beta}^{(+)J} - \delta\rho_{\alpha\beta}^{(-)J} \right),$$

(5)

where the finite-temperature forward- and backward-going amplitudes $\delta\rho_{\alpha\beta}^{(\pm)}$ are related to the corresponding zero-temperature amplitudes X and Y through

$$\delta\rho_{\alpha\beta}^{(+)} = X_{\alpha\beta} f_\beta (1 - f_\alpha) + Y_{\beta\alpha} f_\alpha (1 - f_\beta),$$

(6)

$$\delta\rho_{\alpha\beta}^{(-)} = Y_{\alpha\beta} f_\beta (1 - f_\alpha) + X_{\beta\alpha} f_\alpha (1 - f_\beta).$$

(7)

The nucleon Fermi-Dirac function,

$$f_\alpha = \frac{1}{1 + e^{\frac{\epsilon_\alpha - \mu}{k_B T}}},$$

(8)

where ϵ_α are the single-nucleon energies and μ is the chemical potential, satisfies $\sum_\alpha f_\alpha = A$.

It should be noted that the condition whether electron capture on a specific target nucleus releases energy ($Q > 0$) or requires additional external input of energy ($Q < 0$) constrains the energy available to reach various excited states. In order to minimize uncertainties coming from the calculations of the Q value, we compute it from the experimental masses [24]: $Q = M_f - M_i$ (where M_i and M_f are the masses of the parent and daughter nucleus, respectively), as in Ref. [15].

The electron-capture rate is then computed from the electron-capture cross section [12],

$$\lambda^{\text{ec}}(T) \, [\text{s}^{-1}] = \frac{V_{ud}^2 \, g_V^2 \, c}{\pi^2 (\hbar c)^3} \int_{E_{\min}}^\infty \sigma(E_e, T) \, E_e \, p_e c \, f_e(E_e) \, dE_e,$$

(9)

where V_{ud} is the up-down element in the Cabibbo-Kobayashi-Maskawa (CKM) quark mixing matrix, $g_V = 1$ is the weak vector coupling constant, $E_{\min}$ is the threshold energy for electron capture, and $p_e c = (E_e^2 - m_e^2 c^4)^{1/2}$ is the electron momentum. Under stellar conditions encountered in core-collapse supernova, the electron distribution function f_e is well represented by a Fermi-Dirac distribution,

$$f_e = \frac{1}{1 + e^{\frac{E_e - \mu_e}{k_B T}}},$$

(10)

where the electron chemical potential μ_e is determined from the baryon density ρ by inverting the relation:

$$\rho Y_e = \frac{1}{\pi^2 N_A} \frac{1}{(\hbar c)^3} \int_0^\infty [f_e(E_e) - f_{e^+}(E_e)] \, (p_e c)^2 \, d(p_e c),$$

(11)

where N_A is Avogadro's number. The positron distribution function, f_{e^+}, is given by the Fermi-Dirac distribution, Eq. (10), as for the electrons, with $\mu_{e^+} = -\mu_e$. We assume that the phase space is not blocked by neutrinos, i.e., we set $f_\nu = 0$, since neutrinos are expected to escape from the star at least in the first stage of core collapse.

III. ELECTRON-CAPTURE CROSS SECTIONS

In this section we present the results for the electron-capture cross sections on ^{54,56}Fe and $A = 70$–80 Ge isotopes, obtained in the FTSHF + FTRPA model. We compare our results with those calculated from other approaches. In this paper, the analysis is performed for a representative set of Skyrme functionals: SLy4 [25], SGII [26], SkM* [27], and BSk17 [28]. Starting from the original Skyrme functional [29], more than 100 different Skyrme parametrizations have been proposed, often with different subsets of terms accounting for additional density or momentum dependencies of the interaction. Since in the present approach both the Hartree-Fock equations and the RPA matrix equations are based on the same Skyrme

functional, the model is completely determined by the choice of the functional. However, since low-lying states are quite sensitive to the details of the single-particle spectra around the Fermi surface and those details cannot be easily attributed to a single feature of the Skyrme functional, it is difficult to determine which Skyrme force is preferable. Therefore, we have singled out a few parameter sets, among those which have been widely used, in order to provide an estimate of the theoretical uncertainty inherent in the method. To be more precise, SkM* is a typical example of first-generation Skyrme sets, SGII is its descendant and it is supposed to give a better description of spin modes, SLy4 is one of the well-known last-generation Lyon sets, and BSk17 is the functional which reproduces so far at best the empirical masses. We have also checked that the energy of the peak of the GT$^+$ for ^{56}Fe obtained with the selected Skyrme forces lies within or rather close to the experimental range [5].

In Ref. [15], electron-capture cross sections for selected nuclei in the iron mass region and for neutron-rich Ge isotopes were already computed for different Skyrme interactions. Here, in addition, we perform a more systematic comparison with other calculations in the literature regarding the dependence of the cross sections on the temperature and the neutron excess in Fe and Ge nuclei.

A. Iron isotopes

In Fig. 1 the electron-capture cross sections for ^{54,56}Fe for $T = 0.5$, 1.0, and 2.0 MeV are displayed as a function of the incident electron energy. The results for the Skyrme forces SLy4, SGII, SkM*, and BSk17 are shown together with those obtained by the SMMC [30] and the FTRRPA [16] calculations. We first notice that the threshold for the electron capture is slightly shifted toward lower electron energies when the temperature increases. We also note the low electron energy threshold in the case of ^{54}Fe. This is due to the small Q value
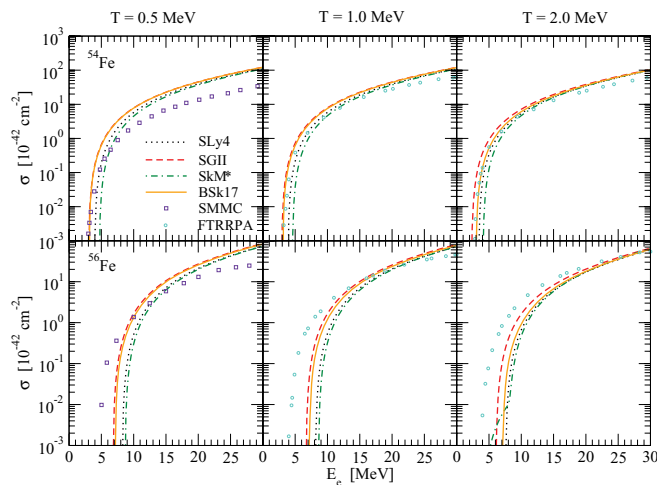

FIG. 1. (Color online) Electron-capture cross sections for ^{54,56}Fe for various temperatures as a function of the incident electron energy, for the Skyrme forces SLy4, SGII, SkM*, and BSk17. The FTSHF + RPA results are compared with cross sections obtained by the SMMC [30] and the FTRRPA [16] calculations.

of the reaction ^{54}Fe $(e^-, \nu_e)^{54}$Mn: $Q = -0.697$ MeV, while for ^{56}Fe $(e^-, \nu_e)^{56}$Mn the nuclear Q value of the reaction is $Q = -3.696$ MeV. In all the calculations for the cross sections presented here, all multipole transitions $J^\pi = 0^\pm$, $1^\pm$, and $2^\pm$ have been considered, while the SMMC calculations include only the GT operator. However, it has been noticed (see, e.g., Fig. 7 in Ref. [15] or Fig. 3 in Ref. [16]) that in the case of ^{56}Fe, up to 30 MeV, the cross section is completely dominated by the 1^+ transition. Note also that in Ref. [30] only the $0\hbar\omega$ GT transition strength is taken into account and not the total strength in the 1^+ channel. Moreover, the quenching of the total GT strength, experimentally observed, has been reproduced in Ref. [30] by renormalizing the GT matrix elements by a factor 0.8. This is equivalent to reducing the axial-vector coupling constant from its free-nucleon value $g_A = 1.262$ to $g_A = 1.0$, as has been done in Ref. [15] and in the present work. As already pointed out in Ref. [15], the cross sections in Fig. 1 exhibit a sharp increase of several orders of magnitude within the first few MeV above threshold, reflecting the trend of the GT$^+$ distribution, while for electron energy larger than 10 MeV the increase becomes more gradual. Even if the general behavior of the cross sections as a function of the electron energy is in agreement with the SMMC and FTRRPA calculations, the absolute values differ by up to one order of magnitude. Specifically, in the case of ^{54}Fe, the cross sections calculated in the FTSHF + FTRPA model tend to be larger than those calculated by the SMMC method for electron energies $E_e \gtrsim 5$ MeV. On the other hand, our results are quite close to those computed in the FTRRPA framework. The smaller discrepancy at high electron energy might come from the fact that also in Ref. [16] all the multipole transitions up to the $2^\pm$ transitions are included. In the case of ^{56}Fe, the cross sections calculated in the FTSHF + FTRPA model are generally smaller than those computed by the SMMC model at low electron energy, while at high electron energy ($E_e \gtrsim 10$ MeV), the SMMC cross sections are smaller. This may be due to the contribution of higher multipoles, which become important at high electron energy. It has to be noticed that since at low electron energies the cross sections are sensitive to the details of the GT distributions, one expects the SMMC results to be more accurate. Our calculations at $T = 1$ and 2 MeV are generally smaller than those obtained in the FTRRPA framework for $E_e \lesssim 15$ MeV.

B. Germanium isotopes

While the electron capture on iron-group nuclei is important in the pre-supernova phase and in the first phase of collapse, at higher densities and temperatures, electron capture also occurs on heavier and neutron-rich nuclei. In the IPM picture, the GT transitions are forbidden for nuclei with $Z < 40$ and $N \geqslant 40$ [31]. However, it has been shown that GT transitions for these nuclei are unblocked by finite-temperature effects. In Ref. [32], a detailed investigation within the RPA approach was performed, showing that GT transitions are thermally unblocked at $T \sim 1.5$ MeV. Thermal excitations can indeed promote protons into the $g_{9/2}$ orbital or remove neutrons from the pf shells, reallowing GT transitions. Another unblocking
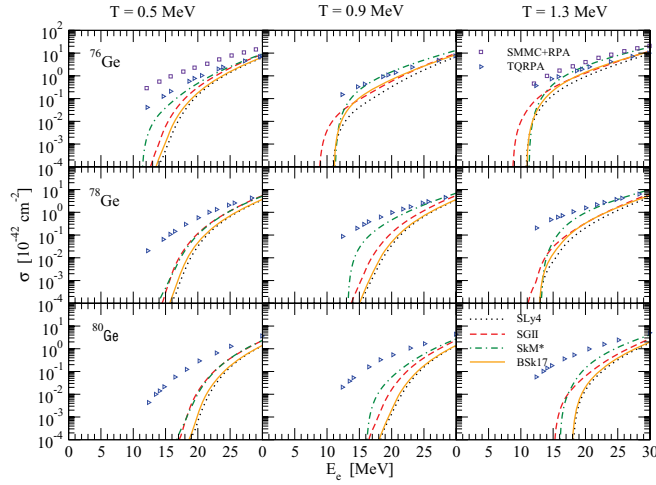
FIG. 2. (Color online) Electron-capture cross sections for ^{76,78,80}Ge for various temperatures as a function of the incident electron energy, for the Skyrme forces SLy4, SGII, SkM*, and BSk17. For comparison, the cross sections obtained by the SMMC + RPA [12] and the TQRPA [17] calculations are also shown.

effect, already present at lower temperatures ($T \sim 0.5$ MeV), is due to configuration mixing between the sdg shell with the pf shell induced by the residual interaction. Within the hybrid model, Langanke *et al.* [12] showed that GT transitions can be unblocked by the configuration mixing in the temperature range $T \sim 0.5$–1.3 MeV, which is relevant for supernova collapse.

In Fig. 2, the electron-capture cross sections for ^{76,78,80}Ge are displayed for $T = 0.5$, 0.9, and 1.3 MeV as a function of the electron energy, together with the results from the hybrid model [12] for ^{76}Ge and $T = 0.5$ and 1.3 MeV, and from the TQRPA [17] calculations. In Fig. 3 the FTSHF + FTRPA results for ^{76,78}Ge are compared with those obtained in the FTRRPA [16] calculations, for $T = 1$ and 2 MeV. In
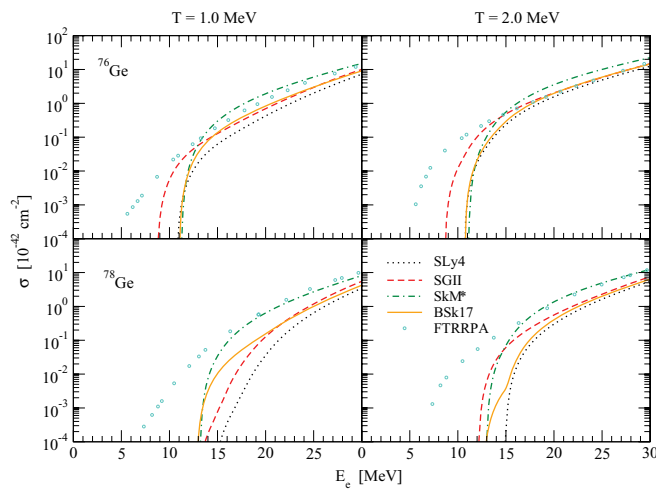

FIG. 3. (Color online) Electron-capture crosssections for ^{76,78}Ge for $T = 1$ and 2 MeV, as a function of the incident electron energy, for the Skyrme forces SLy4, SGII, SkM*, and BSk17. For comparison, the cross sections obtained by the FTRRPA [16] calculations are also shown.
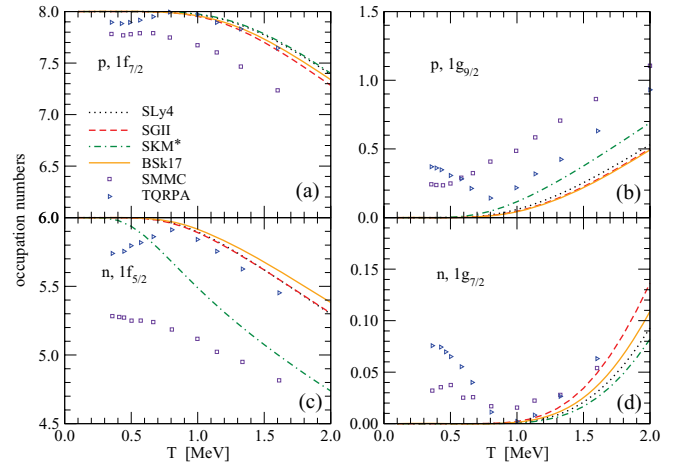

FIG. 4. (Color online) Occupation numbers in ^{76}Ge as a function of temperature for the (a) $1f_{7/2}$ and the (b) $1g_{9/2}$ proton orbitals and for the (c) $1f_{5/2}$ and the (d) $1g_{7/2}$ neutron orbitals. The occupation numbers for the Skyrme forces SLy4, SGII, SkM*, and BSk17 are compared with those obtained by the SMMC and TQRPA models.

both Figs. 2 and 3, the FTSHF + FTRPA cross sections are computed by employing the SLy4, SGII, SkM*, and BSk17 functionals. All the models include the multipole transitions $J^\pi = 0^\pm$, $1^\pm$, and $2^\pm$. The spread of the values obtained with the Skyrme parametrizations differs within an order of magnitude. In both Figs. 2 and 3, we note that the FTSHF + FTRPA results are generally smaller than those calculated by other models. The discrepancy is reduced at high electron energies, since at those energies the cross sections are less sensitive to the details of the GT distributions. The strong dependence of the cross sections on the temperature for low incident electron energies corresponds to the thermal unblocking (see, e.g., Figs. 1 and 2 of Ref. [15]). To investigate the differences pointed out by Fig. 2, we consider the single-particle states calculated in the following three models: FTSHF + FTRPA, SMMC + RPA, and TQRPA. In Fig. 4 the occupation numbers in the illustrative case of ^{76}Ge are displayed as a function of temperature for the $1f_{7/2}$ [panel (a)] and the $1g_{9/2}$ [panel (b)] proton orbitals and for the $1f_{5/2}$ [panel (c)] and the $1g_{7/2}$ [panel(d)] neutron orbitals. We compare the occupation numbers for the Skyrme forces SLy4, SGII, SkM*, and BSk17 with those obtained by the SMMC and TQRPA models. We notice that, at very low temperatures, the transition from the $1g_{9/2}^p$ to the $1g_{7/2}^n$ orbital is possible in the SMMC and in the TQRPA models, while it does not give a contribution in the HF case because of Pauli blocking. Indeed, the $1g_{9/2}^p$ orbital is located about 5 MeV above the Fermi level: with SLy4, at $T = 0$, the proton Fermi energy (i.e., the proton chemical potential) is -9.4 MeV while the energy of the $1g_{9/2}^p$ state is -5 MeV. Therefore, we expect it not to be populated at low temperatures and thus to give a small contribution to the total transition probability. On the other hand, SM calculations include correlations beyond particle-hole excitation and can predict a population of the $1g_{9/2}^p$ state at zero temperature. This behavior can therefore explain the smaller cross sections observed in Fig. 2 for the FTSHF + FTRPA calculations with respect to the SMMC and the TQRPA calculations.
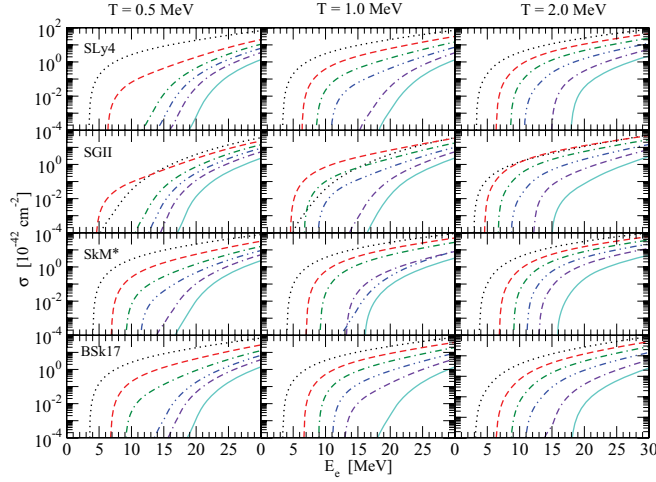
FIG. 5. (Color online) Electron-capture cross sections for Ge $A = 70$–80 isotopes for various temperatures as a function of the incident electron energy, for the Skyrme forces SLy4, SGII, SkM*, and BSk17. The dotted lines correspond to $A = 70$, while the solid lines correspond to $A = 80$, and the other isotopes are between these boundaries.
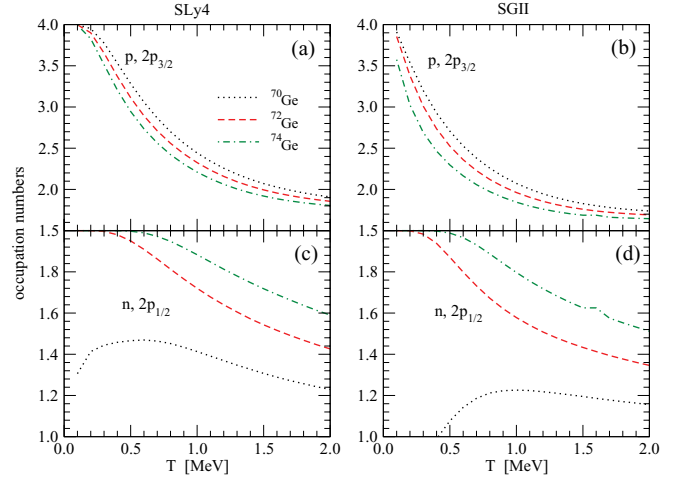

FIG. 6. (Color online) Occupation numbers in ^{70,72,74}Ge as a function of temperature, for the Skyrme forces SLy4 (left panels) and SGII (right panels), for the [(a) and (b)] $2p_{3/2}$ proton orbitals and for the [(c) and (d)] $2p_{1/2}$ neutron orbitals.

In Fig. 5 we illustrate the isotopic dependence of the electron-capture cross section for Ge isotopes. Cross sections for even-even Ge nuclei with $A = 70$–80 are calculated in the FTSHF + FTRPA model and displayed as functions of the incident electron energy, for $T = 0.5$, 1.0, and 2.0 MeV and for the functionals SLy4, SGII, SkM*, and BSk17. The systematic decrease with A of the cross section at given electron energy reflects the increase (in absolute value) of the Q value of the reaction: from $Q = -1.66$ MeV, corresponding to the reaction ^{70}Ge $(e^-, \nu_e)^{70}$Ga, to $Q = -9.99$ MeV, corresponding to the reaction ^{80}Ge $(e^-, \nu_e)^{80}$Ga. Indeed, more-neutron-rich isotopes require more energetic electrons to allow the capture reaction. This implies that, with increasing A, the threshold for the electron-capture increases, and the cross sections are smaller at a given electron energy. The same trend has been observed in Fig. 8 of Ref. [15] for Ni isotopes and in Fig. 4 of Ref. [30] for iron group isotopes.

We notice the different behavior of the cross sections in $^{70-74}$Ge in the case of the SGII force. Indeed, the curves in Fig. 5 corresponding to ^{70}Ge and ^{72}Ge cross each other, breaking the trend observed for all other forces. This can be explained by considering the transition from the $2p_{3/2}^p$ state to the $2p_{1/2}^p$ state. In Fig. 6, the occupation numbers in the isotopes ^{70,72,74}Ge are shown as a function of temperature, for the Skyrme forces SLy4 (left panels) and SGII (right panels), for the $2p_{3/2}$ proton orbitals [panels (a) and (b)], and for the $2p_{1/2}$ neutron orbitals [panels (c) and (d)]. We observe that, in the case of SGII, the $2p_{3/2}^p$ orbitals are less populated at a given temperature with respect to those obtained with the SLy4 force. The $2p_{3/2}^p \rightarrow 2p_{1/2}^n$ transition, therefore, might give a smaller contribution to the cross sections in the case of SGII than in the case of SLy4. Moreover, the difference in the occupation numbers between the isotopes ^{70}Ge and ^{72}Ge is larger in the case of SGII. This may justify a drop in the cross section for ^{70}Ge with respect to ^{72}Ge and ^{74}Ge for

$T \lesssim 1$ MeV and, as a consequence, a possible crossing among the curves. In the case of SLy4, instead, the difference between the occupation numbers for different isotopes is smaller, and thus the noncrossing of the results can be preserved.

IV. ELECTRON-CAPTURE RATES

In this section we calculate the electron-capture rates for Fe and Ge for typical conditions found in the initial phase of core-collapse supernova. The rates are computed by folding the FTSHF + FTRPA cross sections with the electron Fermi-Dirac distribution, according to Eq. (9). The electron chemical potential entering in Eq. (10) is derived from the matter density by inverting Eq. (11).

A. Iron isotopes

In Fig. 7 the electron-capture rates for ^{54,56}Fe for different stellar conditions as functions of temperature are displayed for the Skyrme forces SLy4, SGII, SkM*, and BSk17. For comparison, the SMMC [9], the FTRRPA [16], and the TQRPA [17] calculations are shown. Overall, even if the rates are computed within rather different models, the results have similar trends. The electron-capture rates increase with temperature and electron density in all the models shown. While at low electron densities ($\rho Y_e = 10^7$ g cm^{-3}) the increase of the rates with temperature is up to three orders of magnitude, going from 0.1 to 1.0 MeV, at higher electron densities the rates increase more slowly. At $\rho Y_e = 10^{10}$ g cm^{-3}, the rates are almost independent of the temperature. Going from ^{54}Fe to ^{56}Fe, the rates decrease, which corresponds to the behavior of the cross sections (see Fig. 1). In the case of ^{56}Fe, the FTSHF + FTRPA rates are generally smaller than the FTRRPA and TQRPA results, reflecting the trend of the cross section. We also point out that in the SMMC calculations only the 1^+ transitions are included.
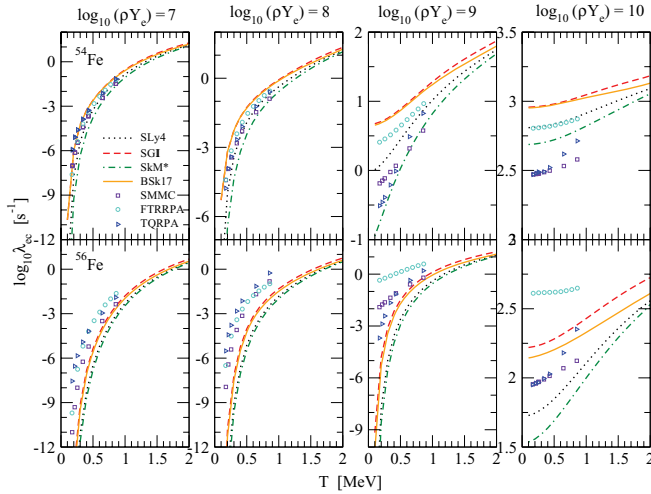
FIG. 7. (Color online) Electron-capture rates for ^{54,56}Fe for different stellar conditions as a function of temperature, for the Skyrme forces SLy4, SGII, SkM*, and BSk17. The FTSHF + RPA results are compared with the rates obtained with the SMMC [9], the FTRRPA [16], and the TQRPA [17] calculations.

B. Germanium isotopes

In Fig. 8 we compare, as a function of temperature, the electron-capture rates for ^{76,78,80}Ge, for different stellar conditions. In all the calculations, the multipole transitions $J^\pi = 0^\pm$, $1^\pm$, and $2^\pm$ have been included. We notice the increasing trend of the rates with increasing temperature and electron density, as for iron isotopes. At high electron density, the rates are almost independent of the temperature. Generally speaking, the FTSHF + FTRPA rates are smaller than the rates calculated within other approaches, reflecting the behavior of the cross sections. The discrepancy among the results obtained in this work and those from other models is reduced with increasing temperature. In the case of ^{76}Ge, the FTRRPA results are in good agreement with the FTSHF + FTRPA results obtained by employing the SGII and the SkM* functional for $\rho Y_e = 10^{10}$ g cm^{-3} and with those obtained
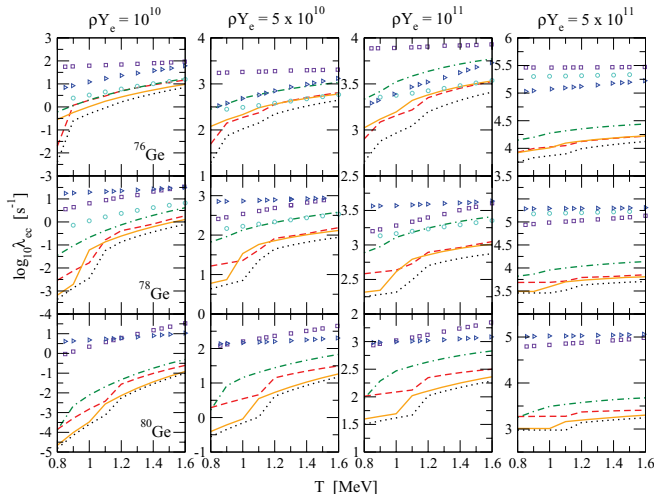
by employing the BSk17 functional for $\rho Y_e = 5 \times 10^{10}$ and 10^{11} g cm^{-3} after 1.2 MeV. The TQRPA results agree very well with the SkM* ones for $\rho Y_e = 5 \times 10^{10}$ g cm^{-3}. In the case of ^{78}Ge, the FTRRPA rates are very close to those obtained with the SkM* functional for $\rho Y_e = 5 \times 10^{10}$ and 10^{11} g cm^{-3}.

It should be noted that with decreasing temperature, the behavior of the electron-capture rates can be in principle nonmonotonic: the cross section drops, because of the closure of the neutron output channels, but the electron density increases and can favor electron capture. There are therefore two opposing effects to be balanced in the integral of Eq. (9): the decrease of the cross section σ with decreasing temperature and electron energy and the slight increase of the electron chemical potential μ_e with decreasing T [see Eq. (11)], which tends to shift the Fermi function f_e to higher electron energy where the cross section is larger.

The results on Fig. 8 allow us to estimate the uncertainties generated by the various microscopic models employed. Within the present Skyrme FTRPA predictions, the spreading of the capture rate is about one order of magnitude. When different approaches such as FTRRPA and TQRPA are also considered, the global uncertainty on the rates is about two orders of magnitude. The one to two order of magnitude differences between the Skyrme interaction results and the TQRPA results may partly arise from the Brink hypothesis. This hypothesis may not be accurate for the individual transitions to states at a low excitation energy (on an absolute scale) in the daughter nucleus, as discussed, e.g., in Ref. [33]. The TQRPA approach avoids this approximation, whereas it is used in the present work.

In Fig. 9 the electron-capture rates for the $A = 70$–80 Ge isotopes are displayed as a function of temperature for the Skyrme functionals SLy4, SGII, SkM*, and BSk17. The rates increase with increasing temperature, but they are almost temperature independent at high electron densities.
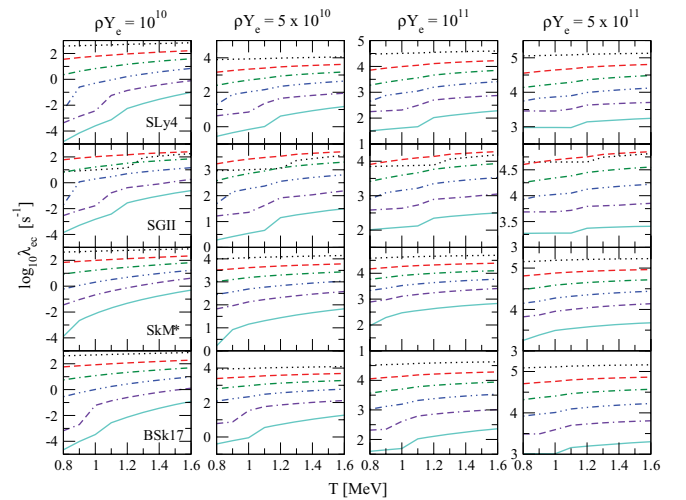

FIG. 8. (Color online) Same as in Fig. 7, but for ^{76,78,80}Ge.

FIG. 9. (Color online) Electron-capture rates for Ge $A = 70$–80 isotopes for different stellar conditions as a function of temperature, for the Skyrme forces SLy4, SGII, SkM*, and BSk17. The dotted lines correspond to $A = 70$, while the solid lines correspond to $A = 80$, and the other isotopes are between these boundaries.

In accordance with the corresponding cross sections (see Fig. 5), at a given temperature and electron density, the rates decrease with increasing A (except in the case of $^{70-74}$Ge with the SGII functional).

V. CONCLUSIONS

Electron-capture rates for stellar conditions have been calculated within a fully self-consistent approach based on Skyrme interactions. The method employed is the finite-temperature Skyrme Hartree-Fock plus finite-temperature charge-exchange RPA. The only input is the Skyrme interaction employed; i.e., both the Skyrme Hartree-Fock and the RPA equations are based on the same functional. Therefore, the scheme is self-consistent. Electron-capture cross section and rate calculations are performed for ^{54,56}Fe and even-even Ge isotopes in the mass range $A = 70$–80.

Our results show a similar trend with respect to other calculations such as the SMMC + RPA, FTRRPA, or TQRPA models, for both the cross sections and the rates. Generally speaking, the present method tends to predict rates that are smaller than those computed from the other approaches. The variety of Skyrme interactions employed and the comparison with previous results obtained within different models allow us to deduce about two orders of magnitude uncertainty on the electron-capture rates. The spread seems to increase with the neutron excess and the electron density. It would be very interesting to compare the capture rates derived in this framework with those inferred from experimental measurements of the GT strength (see, e.g., Refs. [34–36]). This will be considered in a future work.

These results are particularly relevant for astrophysical applications such as core-collapse supernovae theory. Indeed, as demonstrated by several numerical simulations [3,11,37], the evolution of the electron fraction is crucial in supernova dynamics and energetics. As an example, in Refs. [3,37] it has been shown that an increase (reduction) of the electron capture in the denser (outer) regions of the core observed when implementing the SMMC + RPA rates [12] with respect to the IPM model ones leads to a shift of the position of the shock formation inward of about 16% in the core mass and to a 10% smaller velocity across the shock. Moreover, the parameter study of Ref. [38] shows that each increase of the rate of capture by one order of magnitude corresponds roughly to the same decrease ($\sim 0.1 M_\odot$) of the mass of the homologous core.

This corroborates the importance of pursuing this study and generating tables for astrophysical applications, in order to be able to include the FTSHF + FTRPA rates in a numerical simulation. The present work paves the way to more systematic calculations of stellar electron-capture rates. We aim at providing tables for electron-capture rates for a wide range of nuclei of astrophysical interest.

[1] H. A. Bethe, Rev. Mod. Phys. **62**, 801 (1990).

[2] K. Langanke and G. Martínez-Pinedo, Rev. Mod. Phys. **75**, 819 (2003).

[3] H.-T. Janka, K. Langanke, A. Marek, G. Martínez-Pinedo, and B. Müller, Phys. Rep. **442**, 38 (2007).

[4] G. M. Fuller, W. A. Fowler, and M. J. Newman, Astrophys. J. Suppl. Ser. **42**, 447 (1980); **48**, 279 (1982); Astrophys. J. **252**, 715 (1982); **293**, 1 (1985).

[5] S. El-Kateb, K. P. Jackson, W. P. Alford *et al.*, Phys. Rev. C **49**, 3128 (1994).

[6] E. Caurier, K. Langanke, G. Martínez-Pinedo, and F. Nowacki, Nucl. Phys. A **653**, 439 (1999).

[7] T. Suzuki, M. Honma, H. Mao, T. Otsuka, and T. Kajino, Phys. Rev. C **83**, 044619 (2011).

[8] K. Langanke and G. Martínez-Pinedo, Nucl. Phys. A **673**, 481 (2000).

[9] K. Langanke and G. Martínez-Pinedo, At. Data Nucl. Data Tables **79**, 1 (2001).

[10] G. Martínez-Pinedo, K. Langanke, and D. J. Dean, Astrophys. J. Suppl. Ser. **126**, 493 (2000).

[11] A. Heger, K. Langanke, G. Martínez-Pinedo, and S. E. Woosley, Phys. Rev. Lett. **86**, 1678 (2001).

[12] K. Langanke, E. Kolbe, and D. J. Dean, Phys. Rev. C **63**, 032801(R) (2001).

[13] J. M. Sampaio, K. Langanke, G. Martínez-Pinedo, E. Kolbe, and D. J. Dean, Nucl. Phys. A **718**, 440 (2003).

[14] A. Juodagalvis, K. Langanke, W. R. Hix, G. Martínez-Pinedo, and J. M. Sampaio, Nucl. Phys. A **848**, 454 (2010).

[15] N. Paar, G. Colò, E. Khan, and D. Vretenar, Phys. Rev. C **80**, 055801 (2009).

[16] Y. F. Niu, N. Paar, D. Vretenar, and J. Meng, Phys. Rev. C **83**, 045807 (2011).

[17] A. A. Dzhioev, A. I. Vdovin, V. Yu. Ponomarev, J. Wambach, K. Langanke, and G. Martínez-Pinedo, Phys. Rev. C **81**, 015804 (2010).

[18] P. Bonche, S. Levit, and D. Vautherin, Nucl. Phys. A **427**, 278 (1984).

[19] W. Besold, P.-G. Reinhard, and C. Toepffer, Nucl. Phys. A **431**, 1 (1984).

[20] J. S. O'Connell, T. W. Donnely, and J. D. Walecka, Phys. Rev. C **6**, 719 (1972).

[21] J. D. Walecka, in *Muon Physics*, edited by V. M. Hughes and C. S. Wu (Academic, New York, 1975).

[22] J. D. Walecka, *Theoretical Nuclear and Subnuclear Physics* (Imperial College Press and World Scientific, London, 2004).

[23] E. Kolbe, K. Langanke, G. Martínez-Pinedo, and P. Vogel, J. Phys. G **29**, 2569 (2003).

[24] G. Audi G., A. H. Wapstra, and C. Thibault, Nucl. Phys. A **729**, 337 (2003).

[25] E. Chabanat, P. Bonche, P. Haensel, J. Meyer, and R. Schaeffer, Nucl. Phys. A **627**, 710 (1997).

[26] N. Van Giai and H. Sagawa, Nucl. Phys. A **371**, 1 (1981).

[27] J. Bartel, P. Quentin, M. Brack, C. Guet, and H.-B. Hakansson, Nucl. Phys. A **386**, 79 (1982).

[28] S. Goriely, N. Chamel, and J. M. Pearson, Phys. Rev. Lett. **102**, 152503 (2009).

[29] T. H. R. Skyrme, Philos. Mag. **1**, 1043 (1956).

[30] D. J. Dean, K. Langanke, L. Chatterjee, P. B. Radha, and M. R. Strayer, Phys. Rev. C **58**, 536 (1998).

[31] G. M. Fuller, Astrophys. J. **252**, 741 (1982).

[32] J. Cooperstein and J. Wambach, Nucl. Phys. A **420**, 591 (1984).

[33] K. Langanke and G. Martínez-Pinedo, Phys. Lett. B **453**, 187 (1999).

[34] A. L. Cole *et al.*, Phys. Rev. C **74**, 034333 (2006).

[35] N. Anantaraman *et al.*, Phys. Rev. C **78**, 065803 (2008).

[36] G. W. Hitt *et al.*, Phys. Rev. C **80**, 014313 (2009).

[37] K. Langanke, G. Martínez-Pinedo, J. M. Sampaio, D. J. Dean, W. R. Hix, O. E. B. Messer, A. Mezzacappa, M. Liebendörfer, H.-Th. Janka, and M. Rampp, Phys. Rev. Lett. **90**, 241102 (2003).

[38] W. R. Hix, O. E. B. Messer, A. Mezzacappa, J. M. Sampaio, K. Langanke, G. Martínez-Pinedo, M. Liebendörfer, and D. J. Dean, Nucl. Phys. A **758**, 31c (2005).